Inversion of Sea Surface Currents From Satellite-Derived SST-SSH Synergies With 4DVarNets

Ronan Fablet, Bertrand Chapron, J. Le Sommer, Florian Sévellec

AGU ADVANCING EARTH AND SPACE SCIENCES

JAMES | Journal of Advances in Modeling Earth Systems®

RESEARCH ARTICLE
10.1029/2023MS003609

Special Collection:
Machine learning application to Earth system modeling

Inversion of Sea Surface Currents From Satellite-Derived SST-SSH Synergies With 4DVarNets

R. Fablet[1,2], **B. Chapron**[2,3], **J. Le Sommer**[4], **and F. Sévellec**[2,5]

[1]Lab-STICC, IMT Atlantique, Brest, France, [2]ODYSSEY, Inria, Rennes, France, [3]Ifremer, LOPS, Brest, France, [4]CNRS, IGE, Grenoble, France, [5]CNRS, LOPS, Brest, France

Abstract Satellite altimetry offers a unique approach for direct sea surface current observation, but it is limited to measuring the surface-constrained geostrophic component. Ageostrophic dynamics, prevalent at horizontal scales below 100 km and time scales below 10 days, are often underestimated by ocean reanalyzes employing data assimilation schemes. To address this limitation, we introduce a novel deep learning scheme, rooted in a variational data assimilation formulation with trainable observations and a priori terms, that harnesses the synergies between satellite-derived sea surface observations, namely sea surface height (SSH) and sea surface temperature (SST), to enhance sea surface current reconstruction. Numerical experiments, conducted using realistic simulations, in a case study area of the Gulf Stream, demonstrate the potential of the proposed scheme to capture ageostrophic dynamics at time scales of 2.5–3.0 days and horizontal scales of 0.5°–0.7°. The analysis of diverse observation configurations, encompassing nadir along-track altimetry, wide-swath SWOT (Surface Water and Ocean Topography) altimetry, and SST data, highlights the pivotal role of SST features in retrieving a significant portion of the ageostrophic dynamics (approximately 47%). These findings underscore the potential of deep learning and 4DVarNet schemes in improving ocean reanalyzes and enhancing our understanding of ocean dynamics.

Plain Language Summary Satellite altimetry provides a unique means for direct observation of sea surface currents, but it is confined to the geostrophic component, limiting the recovery of a substantial portion of mesoscale sea surface currents in operational products. To address this limitation, we present a novel deep learning framework, rooted in a variational data assimilation paradigm, that unlocks new avenues for leveraging the synergistic relationships between satellite-derived sea surface observations, namely sea surface height and sea surface temperature. This innovative scheme demonstrates its remarkable potential to enhance sea surface current reconstruction and recover a substantial portion of the elusive ageostrophic dynamics. Numerical experiments, employing realistic simulations, in a case study area along the Gulf Stream, underscore the efficacy of our proposed approach. These findings support the pivotal role of physics-informed deep learning in maximizing the utilization of available multimodal observation data sets and numerical simulations to elucidate partially observed sea surface dynamics.

Key Points:

- We present end-to-end deep learning schemes to improve the reconstruction of total sea surface currents from satellite-derived observations
- Experiments in a region of the Gulf Stream support the synergistic analysis of sea surface temperature and sea surface height data
- The strain of sea surface dynamics is a proxy of the uncertainty of the retrieved estimation

Correspondence to:
R. Fablet,
ronan.fablet@imt-atlantique.fr

Citation:
Fablet, R., Chapron, B., Le Sommer, J., & Sévellec, F. (2024). Inversion of sea surface currents from satellite-derived SST-SSH synergies with 4DVarNets. *Journal of Advances in Modeling Earth Systems*, *16*, e2023MS003609. https://doi.org/10.1029/2023MS003609

Received 19 JAN 2023
Accepted 28 APR 2024

Author Contributions:
Conceptualization: R. Fablet, B. Chapron, J. Le Sommer, F. Sévellec
Formal analysis: R. Fablet, J. Le Sommer
Funding acquisition: R. Fablet
Investigation: R. Fablet
Methodology: R. Fablet, F. Sévellec
Project administration: R. Fablet
Resources: R. Fablet
Software: R. Fablet
Supervision: R. Fablet
Validation: R. Fablet, F. Sévellec
Visualization: R. Fablet

1. Introduction

Satellite altimeters provide the main source of observations to inform sea surface dynamics on a regional and global scale (Chelton et al., 2001). Their scarce space-time sampling of the sea surface generally impedes the reconstruction of spatial scales below 100 km and time scales below 10 days (Ballarotta et al., 2019). Also altimetry can only reconstruct geostrophic velocities. As stressed by simulation and observational studies, the ageostrophic components are however critical features of upper ocean dynamics, for instance regarding vertical mixing properties (Mahadevan & Tandon, 2006) and Lagrangian dynamics at sea surface (Baaklini et al., 2021; Sun et al., 2022).

Retrieving sea surface currents at finer scales with both their geostrophic and ageostrophic components naturally arises as a key challenge. This has motivated a large research effort both in terms of simulation studies (Uchida et al., 2022), observational effort (Ardhuin et al., 2019; Villas Boas et al., 2019), and data assimilation methods (Moore et al., 2019; Storto et al., 2019). Regarding the latter aspect, state-of-the-art approaches mostly rely on the one hand on optimal interpolation approaches (Taburet et al., 2019) and on the other hand on data assimilation schemes combined with ocean general circulation models (Baaklini et al., 2021; Benkiran et al., 2021; Fujii et al., 2019). As mentioned above, both approaches still show limitations in the ability to retrieve fine-scale

Writing – original draft: R. Fablet, F. Sévellec
Writing – review & editing: R. Fablet, B. Chapron, J. Le Sommer, F. Sévellec

patterns, whereas both observation-driven and theoretical studies evidence the interplay between fine-scale sea surface dynamics and some observed processes such as sea surface tracers (Ciani et al., 2021; Isern-Fontanet et al., 2006) and drifters' trajectories (Sun et al., 2022).

From a methodological point of view, data-driven and learning-based schemes have also received a growing attention to solve inverse problems in geoscience (Alvera-Azcárate et al., 2007; Barth et al., 2020; Lguensat et al., 2017). Especially, deep learning schemes appear as appealing schemes for the reconstruction of sea surface dynamics from irregularly sampled satellite-derived observations (Fablet, Amar, et al., 2021; Fablet et al., 2023; George et al., 2021; Manucharyan et al., 2021). Interestingly, these studies open new research avenues to make the most of available simulation and observation data sets. They also suggest potential breakthroughs through the ability to exploit the synergies between different sea surface observational fields with no explicitly known relationship (Fablet et al., 2023).

In this study, we exploit these recent methodological advances to explore satellite-derived SST-SSH synergies to inform sea surface currents, including their ageostrophic component. We exploit and adapt multi-modal 4DVarNet schemes introduced in Fablet et al. (2023). Through an observing system simulation experiment for a region of the Gulf Stream, our key contributions are four-fold:

1. We stress the potential of physics-informed deep learning schemes to enhance the reconstruction of sea surface currents (SSC). We report a significant improvement compared with SSH-derived SSC using state-of-the-art SSH products such as (Taburet et al., 2019) in terms of resolved space-time scales and mean-square-error metrics.
2. Our results also support wide-swath SWOT (Surface Water and Ocean Topography) altimetry data to improve the reconstruction of SSC fields compared with the sole use of nadir altimetry data, except for the divergent component of the SSC, for which we only report a marginal gain.
3. We emphasize the contribution of SST-SSH synergies to retrieve a significant fraction of the ageostrophic component of the SSC, typically ≈47% in terms of divergence of the SSC fields, with a major contribution of SST features in the spatial scale range of $^1/_{20}°$–$^1/_4°$.
4. We point out that, as hypothesized from theoretical considerations (?), the strain of sea surface dynamics partially explains (≈60%) the time-averaged mean square error of the SSC.

We further discuss the implications of these results in the context of ongoing research efforts toward the monitoring of upper ocean dynamics.

2. Problem Statement

2.1. Geostrophic and Ageostrophic Sea Surface Dynamics

The horizontal momentum equations together with the hydrostatic equilibrium for the vertical momentum and the non-divergence leads to the following set of equations to describe sea surface dynamics:

$$D_t u - fv = -\frac{1}{\rho_0}\partial_x P + \mathcal{F}_x, \tag{1a}$$

$$D_t v + fu = -\frac{1}{\rho_0}\partial_y P + \mathcal{F}_y, \tag{1b}$$

$$0 = -\frac{1}{\rho_0}\partial_z P - \frac{g}{\rho_0}\rho, \tag{1c}$$

$$\partial_x u + \partial_y v + \partial_z w = 0, \tag{1d}$$

where u, v and w are the zonal, meridional, and vertical velocities, respectively, t is time, x, y and z are the longitude, latitude, and depth, respectively, $\rho_{(0)}$ is the (reference) density for seawater, P is the pressure, f is the Coriolis parameter, g is the acceleration due to gravity, $\mathcal{F}_x$ and $\mathcal{F}_x$ are the action of the zonal and meridional viscous forces, respectively, and D_t ($=\partial_t + u\partial_x + v\partial_y + w\partial_z$) is the material derivative.

These equations are often simplified to reflect the geostrophic balance which occurs under the small Rossby number (Ro $\ll$ 1 i.e., inertial terms are negligible), slow dynamics ($\partial_t \to 0$ for the horizontal momentum equation), large Péclet number (Pe $\ll$ 1 i.e., viscous terms are negligible), and away from direct forcing. This reads:

$$-fv_g = -\frac{1}{\rho_0}\partial_x P, \tag{2a}$$

$$+fu_g = -\frac{1}{\rho_0}\partial_y P, \tag{2b}$$

where u_g and v_g are the zonal and meridional geostrophic velocities, respectively. This formulation still implies an horizontal divergence, which, using Equation 2 with Equation 1d, reads (for $f \neq 0$):

$$\partial_x u_g + \partial_y v_g = -\frac{\beta}{f} v_g, \tag{3}$$

where β ($=\partial_y f$) accounts for the meridional variation of Earth equivalent rotation rate. Hence, the horizontal momentum equations for the ageostrophic components become:

$$D_t u - f v_a = \mathcal{F}_x, \tag{4a}$$

$$D_t v + f u_a = \mathcal{F}_y, \tag{4b}$$

where u_a and v_a are the zonal and meridional ageostrophic velocities, respectively. This last set of equations show the complexity of the ageostrophic components through the action of viscous terms and of the full inertial terms in Equation 2, compared to the rather simple linear relationships between pressure gradients and geostrophic velocities in Equation 2. It is worth noting that boundary conditions, such as observed at the ocean surface, occurred though the actions of the viscous terms ($\mathcal{F}_x$ and $\mathcal{F}_y$). This further suggests the key role of the ageostrophic terms when studying the surface velocities.

In the subsequent sections, for the sake of simplicity, we will refer to geostrophically derived sea surface velocities from SSH fields from Equation 2 using SSH $= (P|_{z=0} - P_{\text{atm}})/g\rho_s$ [where $P|_{z=0}$ is the pressure at the geoid ($z = 0$), P_{atm} is the atmospheric pressure, and ρ_s is the assumed-vertically-constant density of the surface layer] as SSH-derived sea surface currents. Assuming that the $P_{\text{atm}} \ll P|_{z=0}$ and $\rho_s \simeq \rho_0$, we find the simple expression for the surface geostrophic velocities:

$$-fv_g\big|_{z=0} = -g\partial_x \text{SSH}, \tag{5a}$$

$$+fu_g\big|_{z=0} = -g\partial_y \text{SSH}. \tag{5b}$$

As satellite altimeters provide direct satellite-derived measurements of the SSH, we consider these SSH-derived sea surface velocities as baselines for evaluation purposes.

2.2. Data Assimilation for Sea Surface Dynamics

Classically, one states inverse problems in geoscience (Evensen, 2009) as data assimilation problems through some underlying state-space formulation

$$\begin{cases} \dfrac{\partial \mathbf{x}(t)}{\partial t} &= \mathcal{M}(\mathbf{x}(t)) + \eta(t) \\ \mathbf{y}_m(t) &= \mathcal{H}_m(\mathbf{x}(t)) + \epsilon_m(t), \forall\, t, m \end{cases} \tag{6}$$

where $\mathbf{x}$ is the space-time process to be reconstructed and $\mathbf{y}_m$ is an observation process which relates to state $\mathbf{x}$ through observation operator $\mathcal{H}_m$ for observation modality m. When dealing with irregularly sampled

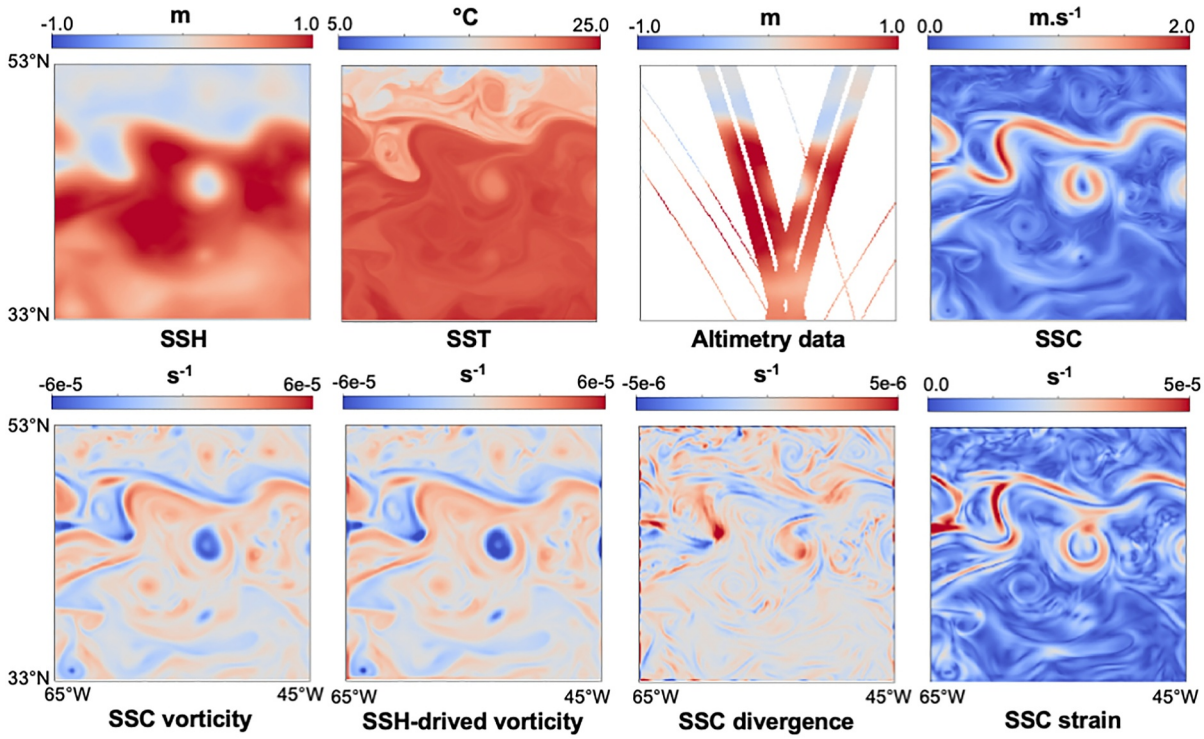

Figure 1. Illustration of the considered case-study using NATL60 simulation data set: first row, from left to right, NATL60 SSH field on November 12th, associated SST field and SSH observation data from nadir and wide-swath SWOT altimeters, SSC field. The second row depicts the vorticity fields for the total currents and SSH-geostrophically-derived ones along with the divergence and strain of the total currents.

observations, operator $\mathcal{H}_m$ accounts for sampling masks. Processes η and ϵ refer to random processes to account for modeling uncertainties and observation noise, respectively. $\mathcal{M}$ refers to the dynamical prior on state x. Given this state-space formulation, the data assimilation problem for the reconstruction of state x given observation data $\{y_k\}_k$ comes to the resolution of a minimization problem. Especially, the variational data assimilation generally leads to:

$$\hat{\mathbf{x}} = \arg\min_{\mathbf{x}} \sum_m \lambda_m \left\| \mathbf{y}_m - \mathcal{H}_m(\mathbf{x}) \right\|^2 + \gamma \left\| \mathbf{x} - \Phi_{\mathcal{M}}(\mathbf{x}) \right\|^2 \tag{7}$$

with $\{\lambda_m\}_m$ and γ Lagrangian multipliers, $\Phi_{\mathcal{M}}(\mathbf{x})$ the time-stepping operator to propagate one-step-ahead state $\mathbf{x}$ at time t to time $t + \Delta t$ based on dynamical prior $\mathcal{M}$. In the above formulation, we consider a matrix form and drop the time variable such that the norms are evaluated as a sum over a given time interval $[0, T]$ according to time step Δt, for example, $\mathbf{x} = \mathbf{x}(0), \mathbf{x}(\Delta t), \ldots, \mathbf{x}(T)$. Given dynamical prior $\mathcal{M}$ and observation operators $\{\mathcal{H}_m\}_m$, data assimilation methods provide different algorithms (Carrassi et al., 2018; Evensen, 2009) to solve this minimization problem especially using adjoint-based gradient descent schemes and Kalman methods. Formulation Equation 7 also relates to Optimal interpolation (Cressie & Wikle, 2015) when considering a single observation term with a masking operator and a prior given by a Gaussian process. Under these hypotheses, one can derive the analytical solution of the resulting linear-quadratic variational cost.

The state-of-the-art methods for the reconstruction of sea surface dynamics from satellite-derived observations rely on such data assimilation schemes. On the one hand, the reconstruction of geostrophic sea surface currents can be stated as the space-time interpolation of satellite altimetry data (Taburet et al., 2019). In such interpolation settings (Le Guillou et al., 2020; Taburet et al., 2019), state $\mathbf{x}$ in Equation 6 refers to a time series of SSH fields and altimetry data (see Figure 1 for an illustration) are the only source of observation data. The observation term in Equation 7 then involves a masking operator to account for the sampling at sea surface of satellite altimeters. While optimal interpolation relates to a covariance-based formulation for term $\|\mathbf{x} - \Phi(x)\|^2$ in Equation 7, an alternative approach relies on assimilation schemes with a simplified prior on sea surface dynamics, which only

depends on sea surface velocities. Quasi-geostrophic (QG) dynamics are examples of such priors (Le Guillou et al., 2020; Ubelmann et al., 2014). Importantly, these interpolation schemes only retrieve geostrophic sea surface velocities and cannot recover ageostrophic components. By contrast, the assimilation of satellite altimetry and satellite-derived SST observations, possibly complemented by other data sources, in ocean general circulation models (OGCM) (Benkiran et al., 2021; Fujii et al., 2019) aim at reconstructing the whole ocean state, including the total sea surface currents. In such data assimilation schemes, operator $\Phi_{\mathcal{M}}$ in Equation 7 implements the time stepping of the OGCM and observation operators $\mathcal{H}_m$ typically encodes the masking operator of the different sources of gappy satellite-derived and in situ data. Such data assimilation schemes often show some limitations in their ability to fully exploit the space-time resolution of available observation data sets compared with the above-mentioned interpolation schemes (Beauchamp, Febvre, et al., 2023; Le Guillou et al., 2020).

Recently, a rich literature has emerged to bridge data assimilation and deep learning (Abdalla et al., 2021; Barthelemy et al., 2021; Bocquet et al., 2020; Boudier et al., 2020; Fablet, Chapron, et al., 2021; Nonnenmacher & Greenberg, 2021). It provides new minimization schemes as well as new means to explore data assimilation problems when the observation operators and/or the dynamical priors are not explicitly known. As such, it opens new avenues to balance the complexity of the inversion problem and the genericity of the underlying variational formulation in Equation 7. Here, as detailed in the subsequent, we benefit from the generic 4DVarNet framework introduced in (Fablet, Chapron, et al., 2021) and explore a learning-based data assimilation schemes for the reconstruction of sea surface currents from multimodal satellite-derived observations.

3. Data

3.1. Case-Study Region and NATL60 Data

The considered case study focuses on a $10° \times 10°$ region between (33°N, 65°W) and (43°N, 55°W). As illustrated in Figure 1, this region involves the main meander of the Gulf Stream as well as a variety of mesoscale eddies and finer-scale sub-mesoscale filaments. It also comprises clear divergent features associated with the ageostrophic flow component, which makes it suitable for the current study.

The considered simulation data set relies on a nature run of the NATL60 configuration of the NEMO (Nucleus for European Modeling of the Ocean) model (Madec et al., 2022). This simulation delivers a realistic hindcast simulation of ocean dynamics, including mesoscale-to-submesoscale ocean dynamics (Ajayi et al., 2020), over 1 year from October 2012 to September 2013 for a North Atlantic domain with a 1/60° and hourly resolution. The initial and open boundary conditions rely on GLORYS2v3 ocean reanalysis and the atmospheric forcing is based on DFS5.2 (Dussin et al., 2018). We refer the reader to (Ajayi et al., 2020) for a more detailed description and analysis of NATL60 simulation. It has been used in numerous studies regarding the reconstruction and observability of sea surface dynamics (see below for the related OSSE data challenge stated in Le Guillou et al. (2020)).

3.2. OSSE Setting

Our numerical experiments exploit an Observing System Simulation Experiment (OSSE). We rely on the OSSE setting (https://github.com/ocean-data-challenges/2020a_SSH_mapping_NATL60) proposed in Le Guillou et al. (2020) for the benchmarking of SSH mapping methods in the context of upcoming wide-swath altimetry mission SWOT (Gaultier et al., 2015). For a $^1/_{20}°$ spatial resolution, this OSSE data set comprises daily averaged SSH fields and simulated altimetry data. The latter combine simulated nadir along-track data according to a real 4-altimeter configuration and SWOT altimetry data using SWOT simulator (Gaultier et al., 2015). We may point out that simulated altimetry data are created from hourly SSH fields and do not comprise observation noises. This OSSE data set also includes optimally interpolated SSH fields derived from the simulated altimetry data using DUACS (Data Unification and Altimeter Combination System) (Taburet et al., 2019). DUACS is the operational multimission production system of altimeter data developed by CNES/CLS.

In this study, we complement this initial OSSE data set with two additional data sources with the same $^1/_{20}°$ spatial resolution: the series of daily averaged sea surface currents (SSC) and the series of daily averaged sea surface temperature (SST). We also generate SST observations with resolutions of $^1/_{10}°$, $^1/_{5}°$, $^1/_{4}°$ and $^1/_{2}°$ using coarsening and subsampling operations to provide a more realistic simulations of the diversity of operational Level-4 SST products (Donlon et al., 2012; O'Carroll et al., 2019). We report in Figure 1 an illustration of the considered data

set. We refer the interested reader to (Zhu & Fablet, 2023) to access the resulting OSSE data set. The exploration of SST data follows our previous work (Fablet et al., 2023) and numerous studies (Guimbard et al., 2017; Isern-Fontanet et al., 2006; Klein & Hua, 1990) that support the potential of multimodal synergies between different sea surface variables to inform sea surface dynamics.

For the training configuration, we split the 1-year time series into training, validation, and test data sets according to the following time periods: from 4 February 2013 to 30 September 2013, from 1 January 2013 to 4 February 2013, and from 20 October 2012 to 4 December 2012, respectively.

4. Methods

This Section presents the proposed 4DVarNet scheme for the reconstruction of sea surface currents from satellite-derived SST-SSH synergies. We first detail the considered 4DVarNet architecture before describing our learning scheme.

4.1. Proposed 4DVarNet Scheme

4DVarNet schemes refer to end-to-end neural architectures introduced in (Fablet, Chapron, et al., 2021) to solve data assimilation problems and extended to multimodal inversion schemes in Fablet et al. (2023). As sketched in Figure 2, the proposed 4DVarNet scheme exploits as inputs time series of satellite altimetry data and SST fields and outputs gap-free SSH fields and SSC fields. Importantly, it combines two main components: the definition of an underlying variational formulation similar to Equation 7 and an iterative update rule of the associated trainable gradient-based solver. The latter relies at each iteration on the gradient of the variational cost w.r.t. the state using automatic differentiation tools embedded in deep learning frameworks such as PyTorch (Porch is among the state-of-the-art open source Python package for deep learning. We let the reader refer to https://pytorch.org/ for a description of this Python package). Overall, the 4DVarNet scheme implements a predefined number, typically from 5 to 15, of the iterative update rule to map the input partial observations to the reconstructed sea surface dynamics. We refer the reader to (Fablet, Chapron, et al., 2021) for a detailed presentation of the 4DVarNet framework along with its link to variational data assimilation formulations as well as to our open source code (Fablet & Zhu, 2023) for the detailed parameterization of the different neural components of the 4DVarNet schemes.

Let us formally introduce the considered variational formulation. Let $\mathbf{x}$ denote hereafter the space-time state to be reconstructed, $\mathbf{y}$ the altimetry-derived observations and $\mathbf{z}$ the SST data. The considered variational cost, denoted by $U_{\Phi}(\mathbf{x},\mathbf{y},\mathbf{z})$, is given by:

$$U_{\Phi}(\mathbf{x},\mathbf{y},\mathbf{z}) = \lambda_1 \|\mathbf{y}-\mathbf{x}\|_{\Omega}^2 + \lambda_2 \|\mathcal{G}(\mathbf{x}) - \mathcal{H}(\mathbf{z})\|^2 + \gamma \|\mathbf{x} - \Phi(\mathbf{x})\|^2, \quad (8)$$

where λ_1, λ_2, and γ are Lagrangian multipliers. State $\mathbf{x}$ combines SSH denoted by $\mathbf{x}_{\mathrm{SSH}}$ and SSC, such that $\mathbf{x} = (\mathbf{x}_{\mathrm{SSH}}, \mathbf{x}_{\mathrm{u}}, \mathbf{x}_{\mathrm{v}})$, with $\mathbf{x}_{\mathrm{u}}$ and $\mathbf{x}_{\mathrm{v}}$ the meridional and zonal SSC components. Besides, as in Fablet et al. (2023), we adopt a two-scale decomposition of the SSH fields to explicitly use both raw altimetry data and DUACS interpolation as observation data. We may point out that $\mathbf{y}$ has the same dimension as $\mathbf{x}$ in Equation 8. Here, We apply a regridding of the SSH observations onto the reference 1/20° grid and Ω refers to the masking operator used to account for observation gaps in the altimetry data as well as for the fact that the SSC component is never directly observed (In other words, our current implementation of the proposed 4DVarNet scheme applies to Level-3 and Level-4 data and cannot directly ingest raw Level-2 data. Such extensions would require additional developments to specify the observation operator adapted to Level-2 data in Equation 8) In Figure 2b, we sketch the neural implementation of variational cost Equation 8, which is pivotal in the implementation of the gradient-based optimizer introduced below.

Operators $\mathcal{G}()$ and $\mathcal{H}()$ are trainable operators which aim at extracting relevant features from SST observations z to match features extracted from state x. Following our previous work on SST-SSH synergies (Fablet et al., 2023), we parameterize $\mathcal{G}()$ and $\mathcal{H}()$ as non-linear convolutional networks. They involve a block of three convolutional layers with hyperbolic tangent activations followed by a linear convolutional network and a batch normalization layer. The number of channels (or features) of this last convolutional layer defines the dimension of the multimodal term $\mathcal{G}(\mathbf{x}) - \mathcal{H}(\mathbf{z})$. In our experiments, we exploit a 20-dimensional multimodal feature space.

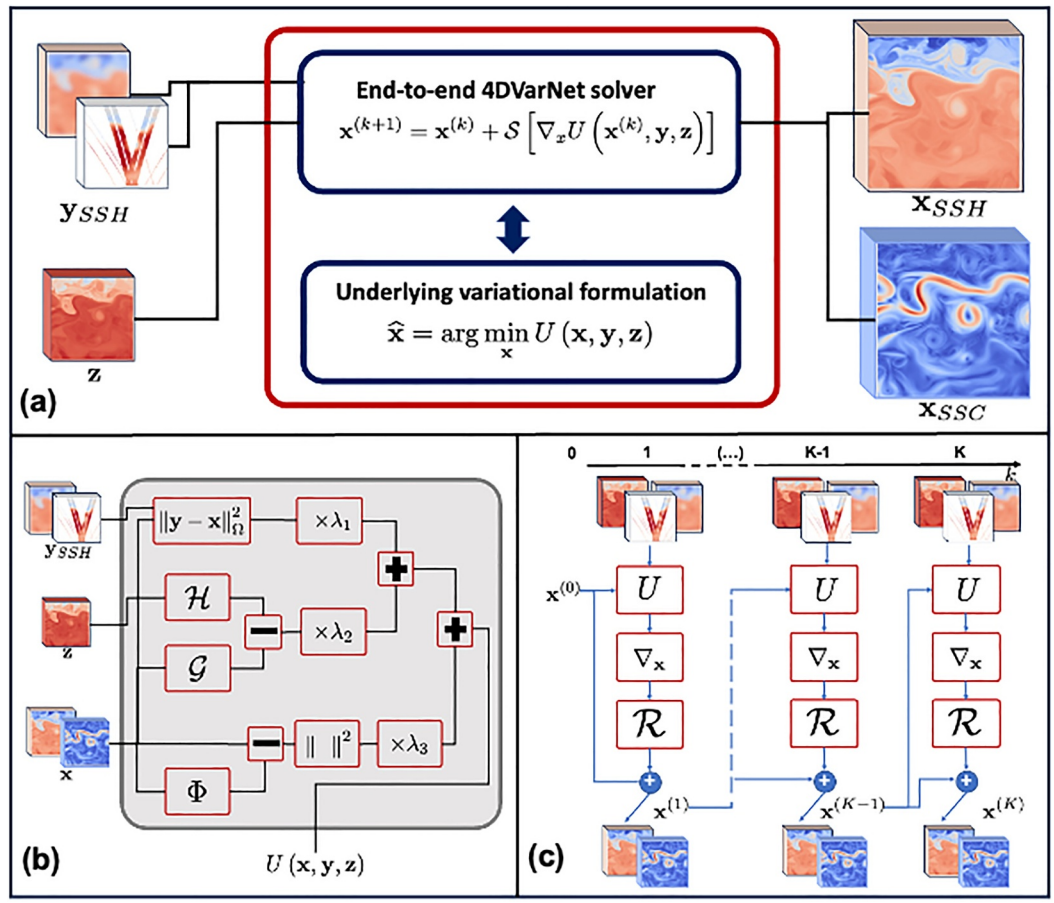

Figure 2. Sketch of the proposed 4DVarNet scheme for the reconstruction of sea surface current fields from SSH and SST observations: (a) Our 4DVarNet scheme provides an end-to-end neural architecture to reconstruct SSH fields $\mathbf{x}_{SSH}$ and SSC fields $\mathbf{x}_{SSC}$ from satellite-derived SSH data $\mathbf{y}_SSH$ and SST observations $\mathbf{z}$. The SSH observations comprise the optimally interpolated SSH product (Taburet et al., 2019) and the actual gappy satellite-derived SSH measurements. For the sake of simplicity, we only depict in this figure the norm of the SSC fields and not their zonal and meridional components; (b) Neural implementation of variational cost $U(\mathbf{x}, \mathbf{y}, \mathbf{z})$ Equation 8 which we rely on to state the reconstruction problem as a minimization issue. It involves three convolutional networks, namely Φ a prior on the underlying space-time dynamics of state $\mathbf{x}$ and operators $\mathcal{G}$ and $\mathcal{H}$ in a multimodal observation term between SST fields $\mathbf{z}$ and state $\mathbf{x}$ (see Equation 8); (c) unfolded representation of the 4DVarNet scheme which implements K iterations of a gradient-based minimization of variational cost $U(\mathbf{x}, \mathbf{y}, \mathbf{z})$ according to Equation 9. ∇_x refers to the automatic differentiation operator natively embedded in deep learning framework and $\mathcal{R}$ to a recurrent neural network, here a LSTM (LeCun et al., 2015). We refer the reader to the main text for the presentation of the considered 4DVarNet scheme.

Operator Φ states the considered prior onto the space-time dynamics of state $\mathbf{x}$. Within a classic model-driven approach, Φ would refer to the time-stepping operator to forecast future states from an initial condition. Following (Fablet, Chapron, et al., 2021; Fablet et al., 2023), we consider a purely data-driven parameterization with a two-scale U-Net architecture (Cicek et al., 2016). It relates to a projection-based parameterization of the prior and led to better performance in previous numerical experiments for both Lorenz's systems (Fablet, Chapron, et al., 2021) and SSH mapping (Beauchamp, Febvre, et al., 2023; Fablet et al., 2023).

As sketched in Figure 2, the considered 4DVarNet schemes implement the following iterative gradient-based solver to minimize variational cost Equation 8:

$$\begin{cases} \mathbf{h}(k+1),\ \mathbf{c}(k+1) = \mathcal{R}\left[\cdot\nabla_x U\left(\mathbf{x}^{(k)}, \{\mathbf{y}, \mathbf{z}\}\right),\ \mathbf{h}(k),\ \mathbf{c}(k)\right] \\ \mathbf{x}^{(k+1)} = \mathbf{x}^{(k)} - \mathcal{L}\left(\mathbf{h}^{(k+1)}\right) \end{cases} \tag{9}$$

with $\mathcal{R}$ a LSTM cell, $\mathcal{L}$ a linear operator, $(\mathbf{h}(k), \mathbf{c}(k))$ the internal state of the LSTM cell at iteration k and $\mathbf{x}^{(k)}$ the reconstructed state at iteration k. As mentioned above, we consider 4DVarNet schemes with 5–15 iterations. The LSTM cell is a 2D-convolutional LSTM cell with 150-dimensional internal states. The considered iterative rule can be regarded as a momentum-based gradient-based descent which has been widely explored for optimizer learning problems (Hospedales et al., 2020).

Overall, the trainable components of the 4DVarNet scheme comprise: operators $\mathcal{G}$ and $\mathcal{H}$, prior Φ, LSTM cell $\mathcal{R}$, and linear mapping $\mathcal{L}$. This amounts to a total number of parameters to be trained from data of about 1.4 M parameters for the considered case-study.

4.2. Learning Setting

We benefit from the end-to-end feature of the considered 4DVarNet scheme to run a supervised strategy. It learns all trainable components with a view to optimizing the reconstruction performance. The training loss then combines reconstruction losses for SSH and SSC fields accounting respectively for the SSH and its gradient, the zonal and meridional components of current state $\mathbf{x}_{\mathrm{SSC}} = (\mathbf{x}_u, \mathbf{x}_v)$, and the divergence of the SSC fields:

$$\mathcal{L}_{\mathrm{SSH}} = \sum_i \left\| \mathbf{x}^{\mathrm{true}}_{\mathrm{SSH},i} - \hat{\mathbf{x}}_{\mathrm{SSH},i} \right\|^2 \tag{10}$$

$$\mathcal{L}_{\nabla\mathrm{SSH}} = \sum_i \left\| \nabla\mathbf{x}^{\mathrm{true}}_{\mathrm{SSH},i} - \nabla\hat{\mathbf{x}}_{\mathrm{SSH},i} \right\|^2 \tag{11}$$

$$\mathcal{L}_{u,v} = \sum_i \left[\left\| \mathbf{x}^{\mathrm{true}}_{u,i} - \hat{\mathbf{x}}_{u,i} \right\|^2 + \left\| \mathbf{x}^{\mathrm{true}}_{v,i} - \hat{\mathbf{x}}_{v,i} \right\|^2 \right] \tag{12}$$

$$\mathcal{L}_{\mathrm{div}} = \sum_i \left\| \partial_x \mathbf{x}^{\mathrm{true}}_{u,i} + \partial_y \mathbf{x}^{\mathrm{true}}_{v,i} - \partial_x \hat{\mathbf{x}}_{u,i} - \partial_y \hat{\mathbf{x}}_{v,i} \right\|^2 \tag{13}$$

where superscript $^{\mathrm{true}}$ (resp. $\hat{}$) refers to the true (resp. reconstructed) SSH or SSC fields. Regarding $\mathcal{L}_{\nabla\mathrm{SSH}}$ and $\mathcal{L}_{\mathrm{div}}$, we compute the gradient and divergence operator using finite-difference approximations parameterized as convolutional layers with known and non-trainable weights. As proposed in (Fablet, Chapron, et al., 2021), we complement these training losses with additional regularization terms

$$\mathcal{L}_{\Phi} = \sum_i \left[\left\| \mathbf{x}^{\mathrm{true}}_i - \Phi\left(\mathbf{x}^{\mathrm{true}}_i\right) \right\|^2 + \left\| \hat{\mathbf{x}}_i - \Phi(\hat{\mathbf{x}}_i) \right\|^2 \right] \tag{14}$$

These regularization terms better constrain the training of prior Φ. Overall, the training loss is the weighted sum of these different losses with relative weights set empirically from cross-validation experiments.

Overall, we implement the 4DVarNet scheme and the associated learning strategy using Pytorch. We use Adam as optimizer with a fixed learning rate of 10^{-3}. After a first training procedure over 200 epochs, we fine-tune the best model over the validation data set over 200 more epochs. We make open source our Pytorch code, including the parameterization of the different neural components and our training setup (Fablet & Zhu, 2023).

4.3. Evaluation Framework and Benchmarked Approaches

Our numerical experiments involve a quantitative evaluation of the reconstruction performance using metrics evaluated over the test data set. We adapt the metrics introduced in Le Guillou et al. (2020) for mapping SSH fields and geostrophic SSC fields (We refer the reader to the following link for the detailed presentation of the evaluation experiment and benchmarked approaches https://github.com/ocean-data-challenges/2020a_SSH_mapping_NATL60), especially:

- $\lambda_{t,u}$ and $\lambda_{t,v}$, the minimum time scale resolved in days for respectively the zonal and meridional velocities;
- $\lambda_{x,u}$ and $\lambda_{x,v}$, the minimum spatial scale resolved in degrees for respectively the zonal and meridional velocities.

Table 1
Synthesis of the Reconstruction Performance of the Benchmarked Approaches: We Report the Performance Metrics of the Benchmarked Approaches for the Reconstruction of Image Time Series of Sea Surface Currents From Satellite Data

Approach	Data used	$\lambda_{x,u}$ (°)	$\lambda_{x,v}$ (°)	$\lambda_{t,u}$ (d)	$\lambda_{t,v}$ (d)	$\tau_{u,v}$	τ_{vort}	τ_{div}	τ_{strain}
True SSH	SSH only	*0.36*	*0.17*	*19.6*	*11.2*	*97.0%*	*96.3%*	*−1.0%*	*92.1%*
DUACS	SSH only	1.72	1.24	12.4	11.6	83.7%	53.5%	−0.5%	24.8%
U-Net	SSH only	1.39	1.22	9.1	10.3	89.1%	72.3%	−3.0%	65.0%
	SSH-SST	1.33	0.90	4.0	4.2	92.6%	79.4%	19.5%	72.0%
4DVarNet	SSH only	0.9	0.7	4.3	5.6	94.0%	86.1%	12.1%	81.3%
(ours)	SSH-SST	**0.76**	**0.61**	**2.7**	**2.5**	**97.4%**	**92.1%**	**46.9%**	**87.2%**

Note. We refer the reader to the main text for the description of the different metrics. We highlight in bold the best score.

As described in Le Guillou et al. (2020), these metrics rely on a spectral analysis. We also evaluate the reconstruction performance in terms of explained variance, respectively:

- $\tau_{u,v}$, the explained variance for the reconstructed SSC;
- τ_{vort}, the explained variance for the vorticity of the reconstructed SSC;
- τ_{div}, the explained variance for the divergence of the reconstructed SSC;
- τ_{strain}, the explained variance for the strain of the reconstructed SSC (Balwada et al., 2021; Okubo, 1970; Weiss, 1991).

The last three metrics characterize the extent to which the reconstructed SSC capture the local deformation tensor of the true velocity fields. Numerically, the computation of the vorticity, divergence, and strain combines a Gaussian filtering and finite difference approximation of the first-order derivatives.

Our numerical experiments evaluate two configurations of the proposed 4DVarNet framework: one using only SSH observation data and the other one exploiting SST-SSH synergies. For benchmarking purposes, we perform a quantitative comparison with respect to the SSH-derived sea surface currents from the true SSH fields and optimally interpolated DUACS ones (Taburet et al., 2019) using the geostrophic approximation introduced in Section 2. We also evaluate direct learning-based inversion schemes based on U-Net architectures (Cicek et al., 2016) to directly map observation data to SSC fields either considering only SSH observation data or jointly SSH and SST observation data.

5. Results

In this Section, we report the considered numerical experiments for the evaluation of the proposed 4DVarNet schemes for the reconstruction of sea surface currents.

5.1. Synthesis of the Benchmarking Experiments

Table 1 compares the performance of the benchmarked schemes. DUACS SSH-derived geostrophic currents (Taburet et al., 2019) provide a baseline performance with reconstruction score in line with those reported for the metrics considered for SSH mapping (Fablet et al., 2023; Le Guillou et al., 2020) with resolved space-time scales above 1° and 10 days. This baseline accounts for more than 80% of the variance of the total current and about 50% of its vorticity and 25% of its strain. The two 4DVarNet schemes clearly outperform this reconstruction performance with resolved space-time scales below 1° and 7 days. The improvement is greater for all metrics when exploiting SSH-SST synergies, for example, 0.76° versus 1.72° for $\lambda_{x,u}$ for the best 4DVarNet configuration, 97.4% versus 83.7% for $\tau_{u,v}$. This is also particularly noticeable for the resolved timescales below 3 days.

Interestingly, with the multimodal 4DVarNet configuration, the metrics for the explained variance of the velocity fields $\tau_{u,v}$ is also better than those of the SSH-derived currents using the true SSH. This is in line with the retrieval of a significant fraction of the divergent component of the currents ($\tau_{\text{div}} \approx 47\%$ in Table 1). The resolved time scales, $\lambda_{t,u}$ and $\lambda_{x,v}$, are also indicators of the relative contribution of the ageostrophic component of the total currents. Whereas SHH-derived currents lead to poorly resolved time scales greater than 11 days, we report values below 3 days for the multimodal 4DVarNet scheme. Similar conclusions hold for the SSH-only version of the

4DVarnet, though to a lesser extent (e.g., $\tau_{\text{div}} \approx 12\%$ in Table 1). This emphasizes the role of SST observations in the retrieval of the ageostrophic component of the total currents. This benchmarking experiment also clearly supports the relevance of 4DVarNet schemes compared with direct learning-based inversion schemes using off-the-shelf deep learning architectures (here, UNets (Cicek et al., 2016)). For instance, we report for all metrics a better reconstruction performance of the 4DVarNet scheme using only altimetry data than that of a direct UNet-based inversion with altimetry and SST inputs.

Figure 3 further illustrates these results through the reconstructed fields on 12 November 2013. This example stresses some strengthening of the sea surface current along the main meander compared with the SSH-derived geostrophic velocities. This is captured by 4DVarNet reconstruction using SSH-SST synergies. They also illustrate the improvement regarding fine-scale patterns which are smoothed by DUACS baseline. The comparison of the vorticity also indicates some correction of the SSH-derived estimation which is revealed by 4DVarNet scheme. Visually, the reconstructed divergence using 4DVarNet schemes recover important features of the true divergence, though finer-scale patterns are lost, which is in line with the performance metrics reported in Table 1. The visual inspection of Figure 3 only reveals small differences between the 4DVarNet schemes using SSH-only data and SSH-SST data, except for the divergent components. This seems in line with Table 1, which suggest differences for the finer scales (below 0.9° and 5.6 days). For instance, the small eddy South East to the large eddy observed in the center of the area on 12 November 2012, reveals such fine-scale differences between the two 4DVarNet reconstructions.

5.2. Impact of SWOT Data

We analyze in Table 2 how SWOT data contribute to the reconstruction of sea surface currents. For the trained 4DVarNet models considered in Table 1, we evaluate their reconstruction performance when considering only nadir altimetry data rather than nadir and SWOT altimetry data as used in the baseline configuration. The availability of wide-swath altimetry data improves all the performance metrics, with the greatest relative for $\lambda_{x,u}$ (0.9° vs. 1.5°) and $\lambda_{t,u}$ (4.3 vs. 6.5 days). When exploiting SSH-SST synergies, we also observe some improvement though smaller, for example, 92.1% versus 90.8% for τ_{vort} and 85.0% versus 87.2% for τ_{strain}. This emphasizes for the considered case-study that SST fields bring most of the relevant information to retrieve the fine-scale patterns of sea surface currents.

5.3. Impact of the Spatial Resolution of the SST Data

As the spatial resolution of satellite-derived SST products depends both on the satellite sensors as well as on the atmospheric conditions, we evaluate here the impact of the spatial resolution of the SST fields onto the reconstruction performance. From the trained mutimodal 4DVarNet, we fine-tune mutimodal 4DVarNet models using downsampled versions of the original SST fields for spatial resolutions ranging from $^1/_{10}°$ to $^1/_2°$ (To conform to our 4DVarNet implementation, where all input fields are provided for the same reference grid, the downsampled versions of the original SST fields involve a coarsening step, a subsampling step and a bicubic reinterpolation onto the reference grid for each spatial resolution). We compare in Table 3 the performance metrics of these models. As expected, the lower the resolution of the SST, the lower the performance. When considering SST data with a $^1/_2°$ resolution, we only significantly improve the reconstruction of the divergent component of the SSC (25.4% vs. 12% when using only altimetry data as reported in Table 1). From a $^1/_4°$ resolution, we report an improvement for all metrics, which is more noticeable for the resolved time scales. This is of key interest for the application to real microwave SST data (O'Carroll et al., 2019). Besides, the clear gain issued from higher-resolution data also supports the potential of multispectral satellite sensors. Overall, Table 3 suggests that the key SST features used to inform sea surface currents relate to horizontal scales between $^1/_{20}°$ and $^1/_4°$.

5.4. Analysis of the Reconstruction Error

We further analyze the reconstruction error and illustrate in Figure 4 the time-averaged mean square error of the total sea surface current over the considered data set from 20 October 2012 to 4 December 2012 for the trained 4DVarNet scheme exploiting SSH-SST synergies. We also report the time-averaged strain of the true velocities along with the time-averaged amplitude of horizontal SST gradients. We observe a better match between error and strain patterns. Quantitatively, the time-averaged strain explains about 60% of the time-averaged error over the

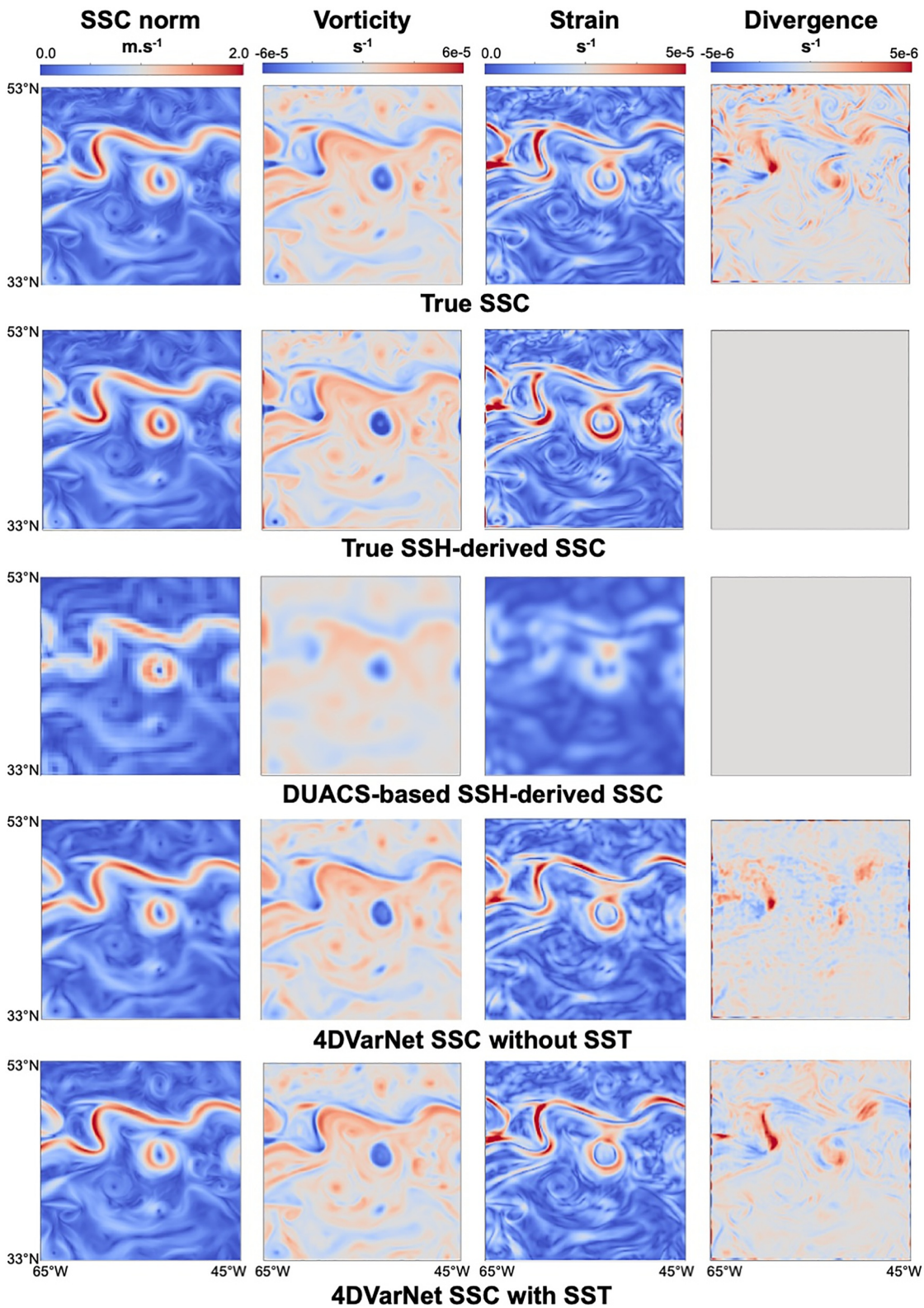

Figure 3. Reconstructed SSC fields on 12 November 2012. From left to right, we depict the norm (i.e., velocity intensity), the vorticity, the divergence and the strain of SSC fields corresponding respectively to, from top to bottom, the true SSC field, the SSH-derived one, DUACS-derived one, and 4DVarNet-derived using only SSH fields and using SSH-SST synergies.

Table 2
Impact of SWOT and SST Data Onto the Reconstruction Performance w.r.t. a Baseline Using Only Nadir Altimetry Data: We Evaluate the Performance Metrics Over the Tests Data Set for the Trained 4DVarNet Schemes Reported in Table 1 When Considering Nadir Altimetry Only (NAlt), Nadir and Wide-Swath SWOT (NAlt + SWOT) Altimetry Combined or Not With SST Data in the Proposed Multimodal Framework

Data	$\lambda_{x,u}$ (°)	$\lambda_{x,v}$ (°)	$\lambda_{t,u}$ (d)	$\lambda_{t,v}$ (d)	$\tau_{u,v}$	τ_{vort}	τ_{div}	τ_{strain}
NAlt	1.5	1.0	6.5	6.4	91.7%	79.0%	8.8%	72.7%
NAlt + SWOT	0.9	0.7	4.3	5.6	94.0%	86.1%	12.1%	81.3%
NALT + SST	0.81	0.62	**2.6**	**2.5**	97.1%	90.8%	46.3%	85.0%
NAlt + SWOT + SST	**0.76**	**0.61**	2.7	2.5	**97.4%**	**92.1%**	**46.9%**	**87.2%**

Note. Bold values show the highest skills.

test data set. We reach similar correlation statistics for the reconstructed strain as expected from the visual similarity between the true and reconstructed strain depicted in Figure 3.

We know that the strain highlights regions of frontogenesis or gradient strengthening (Balwada et al., 2021; Okubo, 1970; Weiss, 1991). It could also be demonstrated that it leads to velocity error growth (Appendix A). This is also consistent with kinetic energy transfer occurring due to the strain of the flow (?). Here we hypothesized that regions of significant error growth (i.e., strain active regions) are more difficult to reconstruct due to their chaotic nature (i.e., small disturbances will become a significant signal). However we do not expect a perfect relation between surface strain and velocity error growth (and so velocity reconstruction error) since other terms, such as viscous terms or sub-surface pressure gradients, also control the velocities, and can become sources of error growth. Interestingly, this analysis is similar for the true strain and the reconstructed one, which could provide a proxy for the quantification of the uncertainty of the reconstruction using 4DVarNet schemes.

6. Discussion

This study has introduced a 4DVarNet deep learning scheme, based on a variational data assimilation formulation, for the reconstruction of sea surface currents from satellite-derived SSH and SST observations. Our numerical experiments support the relevance of this learning-based approach over state-of-the-art schemes to retrieve finer-scale sea surface dynamics (typically 0.5–0.7° and 3 days for the resolved space-time scales), including a significant fraction of the ageostrophic component of the total current (about 47% of the divergence of the SSC). The good skills in the reconstruction of the horizontal divergence of the flow makes it particularly relevant for tracking surface/buoyant polluant concentration (for which convergence regions act as attractors (?)). It is also important for the hypothetic reconstruction of vertical velocities (which vertical gradient is directly related to the horizontal divergence of the flow), with all their dynamical consequences for the export of nutrients, heat, and carbon, for instance. We have also hypothesized, through theoretical arguments, and shown the relation between the flow strain and the error of the reconstructed horizontal velocities. This suggests that strain active regions are good candidates for intense monitoring if one aims to better reconstruct horizontal velocities. We further discuss our contributions according to the following aspects: the monitoring of sea surface velocities, deep

Table 3
Impact of the Spatial Resolution of the SST Observations: We Report the Performance Metrics of the Proposed 4DVarNet Models Using SSH-SST Synergies for SST Observations With Different Spatial Resolutions From 1/20° to 1/2°

SST resolution	$\lambda_{x,u}$ (°)	$\lambda_{x,v}$ (°)	$\lambda_{t,u}(d)$	$\lambda_{t,v}$ (d)	$\tau_{u,v}$	τ_{vort}	τ_{div}	τ_{strain}
$^1/_{20}$°	**0.76**	**0.61**	**2.7**	**2.5**	**97.4%**	**92.1%**	**46.9%**	**87.2%**
$^1/_{10}$°	0.81	0.62	3.0	2.6	96.9%	90.8%	41.8%	85.1%
$^1/_{5}$°	0.87	0.68	3.0	4.4	96.2%	89.0%	37.3%	83.2%
$^1/_{4}$°	0.90	0.70	3.0	3.5	95.6%	87.4%	30.0%	81.5%
$^1/_{2}$°	0.92	0.82	4.3	6.3	94.3%	85.3%	25.4%	80.0%

Note. We refer the reader to the main text for the description of the different metrics. Bold values show the highest skills.

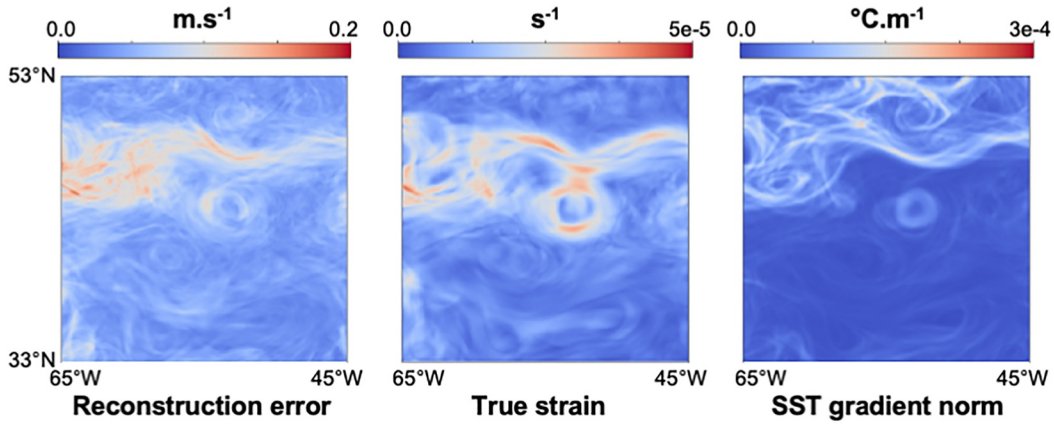

Figure 4. Time-averaged reconstruction error versus mean strain field and SST gradient over the whole test data set: from left to right, we display the time-averaged mean square reconstruction error field of the SSC using the 4DVarNet scheme combining altimetry and SST observations, the time-averaged true strain field and the time-averaged SST gradient. The coefficient of determination between the error field and the later fields is respectively of 59% and 24%. The reconstructed strain field depicted in Figure 3 leads to an explained variance of 57% for the time-averaged reconstruction error.

learning inversions for unobserved upper ocean dynamics and multimodal synergies for ocean monitoring and forecasting.

6.1. Reconstruction of Sea Surface Velocities

Satellite altimetry plays a major role in our ability to monitor sea surface dynamics on a global to local scale. Through the direct measurement of the sea level anomaly, it delivers an estimation of the geostrophic component of sea surface velocities (Chelton et al., 2001). As the scarce sampling of the sea surface by nadir altimeters limits our ability to retrieve dynamical features below ≈1° and 10 days, research effort has been undertaken to observe and reconstruct finer-scale dynamics. In this context, upcoming swide-swath altimetry mission SWOT (Gaultier et al., 2015) will provide the first snapshots of the sea surface height down to a $^1/_{10}°$ spatial resolution. Similarly to nadir altimeters, it will only directly inform the geostropic component of sea surface velocities. Numerous studies (e.g., (Baaklini et al., 2021; Mahadevan & Tandon, 2006)) have evidenced the key role of ageostrophic dynamics in the mesoscale-to-submesoscale range. This has motivated a large research effort toward the exploitation of other observation sources, alone or combined with satellite altimetry, to retrieve sea surface dynamics, including among others SST (Fablet et al., 2018; Isern-Fontanet et al., 2014; Rio et al., 2016), Ocean Color (Ciani et al., 2021), sea surface drifters (Baaklini et al., 2021; Sun et al., 2022), and SAR observations (Chapron et al., 2005). From a methodological point of view, we may distinguish three main categories of approaches: optimal interpolation schemes (Cressie & Wikle, 2015; Taburet et al., 2019), data-driven approaches (Fablet et al., 2017, 2023; Manucharyan et al., 2021), and data assimilation scheme using OGCM (Benkiran et al., 2021; Fujii et al., 2019) or QG dynamical priors (Le Guillou et al., 2020; Ubelmann et al., 2014). The proposed 4DVarNet scheme benefits, on the one hand, from a variational data assimilation formulation to make explicit observation and dynamical priors, especially the expected though unknown relationship between SST and SSC features, and, on the other hand, from the computational efficiency of deep learning schemes, to learn uncalibrated terms and solvers from data in an end-to-end manner. This seems particularly promising to make the most of available multi-source observation data sets for the reconstruction of sea surface currents. Our study supports the ability to retrieve finer-scale patterns than currently achieved by operational products. While our study points out the added-value of wide-swath altimetry data, it suggests that ageostrophic components can be revealed by learning-based schemes from other sea surface tracers sampled at higher-resolution as illustrated with SST fields in our study. This likely relates to specific dynamical regimes in play in the Gulf Stream region (McWilliams et al., 2019; Reul et al., 2014). Especially over oceanic regions displaying large kinetic energy conditions, studies generally report SST-SSH synergies. Both from analytical and numerical (Isern-Fontanet et al., 2006; Klein & Hua, 1990), statistical (Jones et al., 1998; Tandeo et al., 2013) and structural (Le Goff et al., 2016; Turiel et al., 2008) standpoints, strong correlation between SST and SSH patterns are expected. SST patterns certainly often suggest upper ocean motions at different scales. Medium-resolution microwave imagery of the sea surface temperature and

salinity fields can then trace buoyancy surface gradients, with large-scale ocean fronts close to a state of thermal wind balance. However, the surface density (or temperature when salinity is not strongly compensating the link between density and temperature) may only be considered to be a smoothed version of the geostrophic stream function, and the resulting velocity field estimates are likely limited to scales of 50–300 km in the first hundred meters of the water column. Through learning-based schemes and multimodal synergies, our study supports possible extensions to ageostrophic upper ocean dynamics. Key challenges for future work include the exploration of the proposed framework for the variety of dynamical regimes, especially away of Western boundary currents. Although the relationships between partially observed observed sea surface tracers and sea surface dynamics vary according to the dynamical regimes in play (Guimbard et al., 2017; Reul et al., 2014), we expect multimodal deep learning schemes, possibly trained for regime-specific data sets and using transfer learning strategies, to reveal and exploit these multimodal relationships to reconstruct upper ocean dynamics. In this context, the extension to other observation data sets such as drifter trajectories (Baaklini et al., 2021; Sun et al., 2022), SAR observations, as well as multispectral satellite sensors (Barnes et al., 2021; Tilstone et al., 2021; Yurovskaya et al., 2019) and higher-resolution SST observations (Chin et al., 2017) also naturally arises as appealing research directions. Whereas our OSSE provides a noise-free idealized testbed, real altimetry observations involve both observation noises and high-frequency fine-scale geophysical signals, such as internal tides and internal gravity waves (Arbic et al., 2010; Xu & Fu, 2012). Numerous studies support the robustness of deep learning schemes to noisy patterns, when the training data set involves appropriate noise simulations (Shorten & Chin, 2019). Preliminary results for SWOT calibration problems also support the relevance of the proposed approach to account for correlated geophysical noise patterns (Febvre et al., 2022). The availability of realistic tide-resolving submesoscale-permitting ocean simulations provides the basis to address these issues in a future work using the proposed framework. A more challenging task will be the separation of tide-related and tide-free motions at sea surface, which could benefit from an extended version of the proposed neural approach.

6.2. Deep Learning Inversion for Unobserved Upper Ocean Dynamics

Our study further supports the potential for deep learning approaches to reconstruct unobserved or partially observed variables or processes from available satellite-derived and/or in situ observation data sets. The reported case-study for horizontal sea surface currents is in line with recent studies addressing ocean processes, such as ocean eddy heat fluxes (George et al., 2021), tide-related features (Wang et al., 2022), plankton dynamics (Martinez et al., 2020)…The underlying assumption is that deep learning can disentangle the features associated with a given process in available satellite-derived observations. In this context, classic data assimilation schemes require defining explicitly the observation and dynamical operators in play in the underlying state-space formulation Equation 6. Regarding upper ocean dynamics, this generally resorts to considering some discretization of the primitive equations and identity observation operators for ocean state variables and ocean-atmosphere interactions. The complexity of the inversion problem may hinder the ability of these schemes to retrieve fine-scale dynamics when dealing with a poorly constrained observation setting as with the inversion of ocean dynamics from satellite-derived sea surface observations. By contrast, the proposed deep learning scheme focuses only on the ocean variables of interest, here observed and targeted sea surface variables. Through this learning paradigm, we reduce the complexity of the inversion problem and explore the complex relationships exhibited by sea surface tracers governed by upper ocean dynamics. We believe this approach to be generic and relevant to improve our understanding and monitoring of upper ocean dynamics which will remain scarcely observed. In this context, the quantification of inversion uncertainties is also pivotal. In this study, we identified the strain as a potential proxy for uncertainty quantification. Future work could also extend the proposed approach to embed uncertainty quantification in the proposed learning-based inversion scheme (Cheng et al., 2023). This line of work could naturally benefit from bridging variational data assimilation and Bayesian formulation as explored in Beauchamp, Fablet, and Georgenthum (2023) and Lafon et al. (2023).

6.3. OSSEs and Deep Learning to Bridge Ocean Modeling and Multimodal Ocean Remote Sensing

We may also regard the proposed deep learning schemes as alternative means to bridge ocean modeling and ocean observation. Numerous OSSEs have combined simulation data sets and observing systems' simulators for ocean studies (Boukabara et al., 2018; Fujii et al., 2019). They have been widely exploited to assess the potential impact

of new observing systems on the reconstruction and/or forecasting of ocean dynamics. OSSEs in the context of the upcoming SWOT mission fall into this category to evaluate the added-value of wide-swath altimetry data to inform upper ocean dynamics (Benkiran et al., 2021; Ubelmann et al., 2014), as further supported by this study. More recently, OSSEs have provided benchmarking frameworks to intercompare the performance of different approaches for the same task such as space-time interpolation problems for sea surface dynamics (Fablet et al., 2023; Fujii et al., 2019; Le Guillou et al., 2020; Vient et al., 2021). As illustrated here, when dealing with unobserved or scarcely observed processes, OSSEs also provide means to train a model from simulation data sets with a view to applying this model to real data sets. Previous learning-based studies dedicated to the reconstruction of ocean's interior processes, such as for instance the primary production (Puissant et al., 2021) and deep geostrophic currents (Manucharyan et al., 2021), provide such examples. These studies generally learn a mapping from observed gap-free sea surface tracers to the targeted ocean state dynamics. The state-of-the-art performance of neural SSH mapping schemes trained from OSSE data sets (Febvre et al., 2023) also supports extending this approach to the reconstruction of unobserved tracers from irregularly sampled observations. The applicability of this general framework to real observation data sets likely depends on the quality of both the numerical simulations of ocean dynamics and of the simulations of the observing systems. Regarding the later, this study focuses on realistic observation sampling patterns, but does not account for observation noise. While this approach seems relevant for nadir satellite altimetry (Febvre et al., 2023), real SST and SWOT altimetry observations involve more complex and structured noise patterns, that should be addressed in a future work. From a broader perspective, our study advocates to pursue joint research effort between the definition of OSSE data sets and the design and evaluation of deep learning approaches. We believe these aspects to be critical for the development of multimodal observing systems combining satellite-derived observations and in situ data including among others sea surface drifters (Baaklini et al., 2021; Sun et al., 2022), argo profiles (Cossarini et al., 2019; Roemmich et al., 2019), and underwater acoustics data (Storto et al., 2020, 2021).

Appendix A: Velocity Error Growth

Starting from the momentum and nondivergence equations [described in Equation 2] but splitting the velocity (and pressure and viscous terms) in a targeted truth and a small error ($X = \bar{X} + X'$ with $|\bar{X}| \ll |X'|$, where X is any variable) we have:

$$D_t u' - fv' = -u'\partial_x \bar{u} - v'\partial_y \bar{u} - w'\partial_z \bar{u} - \frac{1}{\rho_0}\partial_x P' + \mathcal{F}'_x, \tag{A1a}$$

$$D_t v' + fu' = -u'\partial_x \bar{v} - v'\partial_y \bar{v} - w'\partial_z \bar{v} - \frac{1}{\rho_0}\partial_y P' + \mathcal{F}'_y. \tag{A1b}$$

$$0 = -\frac{1}{\rho_0}\partial_z P' - \frac{g}{\rho_0}\rho', \tag{A1c}$$

$$\partial_x u' + \partial_y v' + \partial_z w' = 0. \tag{A1d}$$

So that error growth reads:

$$\begin{aligned} D_t\left(u'^2 + v'^2\right) = &-(u', v')\begin{pmatrix} \partial_x \bar{u} & \partial_y \bar{u} \\ \partial_x \bar{v} & \partial_y \bar{v} \end{pmatrix}\begin{pmatrix} u' \\ v' \end{pmatrix} \\ &- u'w'\partial_z \bar{u} - v'w'\partial_z \bar{v} - \frac{g}{\rho_0}w'\rho' \\ &- \frac{1}{\rho_0}\left[\partial_x(u'P') + \partial_y(v'P') + \partial_z(w'P')\right] + (u'\mathcal{F}'_x + v'\mathcal{F}'_y), \end{aligned} \tag{A2}$$

where the left handside is the evolution of the error (or error growth), the first line of the right handside is the horizontal transfer of momentum error, the second line of the right handside is the baroclinic transfer of momentum and density errors, and the third line of the right handside is the work of the pressure and viscous force

error. Here the horizontal transfer of momentum error is a scalar product of the erroneous velocities applied to the operator of horizontal targeted-truth-velocity gradient. This could be transformed as:

$$
\begin{aligned}
(u',v')\Sigma\begin{pmatrix}u'\\v'\end{pmatrix} &= \begin{pmatrix}\partial_x\bar{u} & \partial_y\bar{u}\\ \partial_x\bar{v} & \partial_y\bar{v}\end{pmatrix}\begin{pmatrix}u'\\v'\end{pmatrix},\\
&= \frac{1}{2}(u',v')\begin{pmatrix}\Delta+\sigma_n & \sigma_s+\zeta\\ \sigma_s-\zeta & \Delta-\sigma_n\end{pmatrix}\begin{pmatrix}u'\\v'\end{pmatrix},\\
&= \frac{1}{2}(u',v')\begin{pmatrix}\Delta+\sigma_n & \sigma_s\\ \sigma_s & \Delta-\sigma_n\end{pmatrix}\begin{pmatrix}u'\\v'\end{pmatrix},
\end{aligned}
\tag{A3}
$$

where $\Delta = \partial_x\bar{u} + \partial_y\bar{v}$ is the divergence, $\zeta = \partial_x\bar{v} - \partial_y\bar{u}$ is the horizontal vorticity, $\sigma_n = \partial_x\bar{u} - \partial_y\bar{v}$ is the normal strain (or stretching), and $\sigma_s = \partial_x\bar{v} + \partial_y\bar{u}$ is the shear strain (or shearing). This last expression shows the symmetric part of the gradient deformation operator, which is virtually equivalent to the one used for tracer gradient growth (Balwada et al., 2021) in the Okubo-Weiss framework of frontogenesis (Okubo, 1970; Weiss, 1991). It is interesting to note that here the horizontal vorticity (ζ) does not contribute to the error growth, though. Σ can be diagonalized to show the natural growth of the error, which leads to the pair of eigenvalues: $\lambda_{\pm} = \Delta/2 \pm \sigma/2$, where σ is the strain (such as $\sigma^2 = \sigma_n^2 + \sigma_s^2$). Since the horizontal flow is largely strain dominated, this shows that the error growth is controlled by the strain. This result is consistent with energy transfer consideration suggesting the transfer from the mean state (here the targeted-truth) to the eddy field (here the error) following the strain of the flow (?). However note that the total error growth will also be affected by baroclinic error transfers and pressure and viscous work.

Data Availability Statement

We distribute through open source license the data sets considered in the reported experiments (Zhu & Fablet, 2023) as well as our pytorch implementation and trained pytorch models (Fablet & Zhu, 2023). The Pytorch implementation of the proposed 4DVarNet scheme is available here: https://doi.org/10.5281/zenodo.8083903.

Acknowledgments
This work was supported by LEFE program (LEFE MANU and IMAGO projects IA-OAC and ARVOR, respectively), CNES (OSTST DUACS-HR and SWOT ST DIEGO), ANR Projects Melody (ANR-19-CE46-0011) and OceaniX (ANR-19-CHIA-0016) and EU Horizon Europe project EDITO Model Lab (Grant 101093293). It benefited from HPC and GPU resources from Azure (Microsoft Azure grant) and from GENCI-IDRIS (Grant 2021-101030). We thank the reviewers and the associate editor for their thoughtful feedbacks and comments that greatly helped in improving our manuscript.

References

Abdalla, S., Abdeh Kolahchi, A., Andersen, O., Antich, H., Arbic, B., Armitage, T., et al. (2021). Altimetry for the future: Building on 25 years of progress. *Advances in Space Research*, *68*(2), 319–363. https://doi.org/10.1016/j.asr.2021.01.022

Ajayi, A., Le Sommer, J., Chassignet, E., Molines, J.-M., Xu, X., Albert, A., & Cosme, E. (2020). Spatial and temporal variability of the North Atlantic eddy field from two kilometric-resolution ocean models. *Journal of Geophysical Research: Oceans*, *125*(5), e2019JC015827. https://doi.org/10.1029/2019JC015827

Alvera-Azcárate, A., Barth, A., Beckers, J.-M., & Weisberg, R. H. (2007). Multivariate reconstruction of missing data in sea surface temperature, chlorophyll, and wind satellite fields. *Journal of Geophysical Research*, *112*(C3). https://doi.org/10.1029/2006JC003660

Arbic, B., Wallcraft, A., & Metzger, E. (2010). Concurrent simulation of the eddying general circulation and tides in a global ocean model. *Ocean Modelling*, *32*(3), 175–187. https://doi.org/10.1016/j.ocemod.2010.01.007

Ardhuin, F., Brandt, P., Gaultier, L., Donlon, C., Battaglia, A., Boy, F., et al. (2019). SKIM, a candidate satellite mission exploring global ocean currents and waves. *Frontiers in Marine Science*, *6*. https://doi.org/10.3389/fmars.2019.00209

Baaklini, G., Issa, L., Fakhri, M., Brajard, J., Fifani, G., Menna, M., et al. (2021). Blending drifters and altimetric data to estimate surface currents: Application in the Levantine Mediterranean and objective validation with different data types. *Ocean Modelling*, *166*, 101850. https://doi.org/10.1016/j.ocemod.2021.101850

Ballarotta, M., Ubelmann, C., Pujol, M.-I., Taburet, G., Fournier, F., Legeais, J., et al. (2019). On the resolutions of ocean altimetry maps. *Ocean Science*, *15*(4), 1091–1109. https://doi.org/10.5194/os-15-1091-2019

Balwada, D., Xiao, Q., Smith, S., Abernathey, R., & Gray, A. (2021). Vertical fluxes conditioned on vorticity and strain reveal submesoscale ventilation. *Journal of Physical Oceanography*, *51*(9), 2883–2901. https://doi.org/10.1175/JPO-D-21-0016.1

Barnes, B., Hu, C., Bailey, S., Pahlevan, N., & Franz, B. (2021). Cross-calibration of MODIS and VIIRS long near infrared bands for ocean color science and applications. *Remote Sensing of Environment*, *260*, 112439. https://doi.org/10.1016/j.rse.2021.112439

Barth, A., Alvera-Azcárate, A., Licer, M., & Beckers, J.-M. (2020). DINCAE 1.0: A convolutional neural network with error estimates to reconstruct sea surface temperature satellite observations. *Geoscientific Model Development*, *13*(3), 1609–1622. https://doi.org/10.5194/gmd-13-1609-2020

Barthelemy, S., Brajard, J., Bertino, L., & Counillon, F. (2021). Super-resolution data assimilation. *arXiv:2109.08017*. https://doi.org/10.48550/arXiv.2109.08017

Beauchamp, M., Fablet, R., & Georgenthum, H. (2023). Neural SPDE solver for uncertainty quantification in high-dimensional space-time dynamics. *arXiv*. https://doi.org/10.48550/arXiv.2311.01783

Beauchamp, M., Febvre, Q., Georgenthum, H., & Fablet, R. (2023). End-to-end neural interpolation of satellite altimetry data using 4DVarNet schemes. *Geoscientific Model Development*, *16*(8), 2119–2147. https://doi.org/10.5194/gmd-16-2119-2023

Benkiran, M., Ruggiero, G., Greiner, E., Le Traon, P.-Y., Rémy, E., Lellouche, J., et al. (2021). Assessing the impact of the assimilation of SWOT observations in a global high-resolution analysis and forecasting system Part 1: Methods. *Frontiers in Marine Science*, *8*. https://doi.org/10.3389/fmars.2021.691955

Bocquet, M., Brajard, J., Carrassi, A., & Bertino, L. (2020). Bayesian inference of chaotic dynamics by merging data assimilation, machine learning and expectation-maximization. *Foundations of Data Science*, *2*(1), 55–80. https://doi.org/10.3934/fods.2020004

Boudier, P., Fillion, A., Gratton, S., & Gürol, S. (2020). DAN—An optimal Data Assimilation framework based on machine learning Recurrent Networks. *arXiv:2010.09694*.

Boukabara, S., Ide, K., Zhou, Y., Shahroudi, N., Hoffman, R., Garrett, K., et al. (2018). Community global observing system simulation experiment (OSSE) package (CGOP): Assessment and validation of the OSSE system using an OSSE–OSE intercomparison of summary assessment metrics. *Journal of Atmospheric and Oceanic Technology*, *35*(10), 2061–2078. https://doi.org/10.1175/JTECH-D-18-0061.1

Carrassi, A., Bocquet, M., Bertino, L., & Evensen, G. (2018). Data assimilation in the geosciences: An overview of methods, issues, and perspectives. *WIREs Climate Change*, *9*(5), e535. https://doi.org/10.1002/wcc.535

Chapron, B., Collard, F., & Ardhuin, F. (2005). Direct measurements of ocean surface velocity from space: Interpretation and validation. *Journal of Geophysical Research*, *110*(C7). https://doi.org/10.1029/2004JC002809

Chelton, D., Ries, J., Haines, B. J., Fu, L.-L., & Callahan, P. S. (2001). Satellite altimetry. In A. Cazenave & L.-L. Fu (Eds.), *International geophysics* (Vol. 69, pp. 58–64). Academic Press. https://doi.org/10.1016/b978-012374473-9.00340-4

Cheng, S., Quilodrán-Casas, C., Ouala, S., Farchi, A., Liu, C., Tandeo, P., et al. (2023). Machine learning with data assimilation and uncertainty quantification for dynamical systems: A review. *IEEE/CAA Journal of Automatica Sinica*, *10*(6), 1361–1387. https://doi.org/10.1109/JAS.2023.123537

Chin, T., Vazquez-Cuervo, J., & Armstrong, E. (2017). A multi-scale high-resolution analysis of global sea surface temperature. *Remote Sensing of Environment*, *200*, 154–169. https://doi.org/10.1016/j.rse.2017.07.029

Ciani, D., Charles, E., Buongiorno Nardelli, B., Rio, M.-H., & Santoleri, R. (2021). Ocean currents reconstruction from a combination of altimeter and ocean colour data: A feasibility study. *Remote Sensing*, *13*(12), 2389. https://doi.org/10.3390/rs13122389

Cicek, O., Abdulkadir, A., Lienkamp, S., Brox, T., & Ronneberger, O. (2016). 3D U-Net: Learning dense volumetric segmentation from sparse annotation. In *Proceedings of MICCAI* (pp. 424–432).

Cossarini, G., Mariotti, L., Feudale, L., Mignot, A., Salon, S., Taillandier, V., et al. (2019). Towards operational 3D-Var assimilation of chlorophyll Biogeochemical-Argo float data into a biogeochemical model of the Mediterranean Sea. *Ocean Modelling*, *133*, 112–128. https://doi.org/10.1016/j.ocemod.2018.11.005

Cressie, N., & Wikle, C. (2015). *Statistics for spatio-temporal data*. John Wiley & Sons.

Donlon, C. J., Martin, M., Stark, J., Roberts-Jones, J., Fiedler, E., & Xindong, W. (2012). The operational sea surface temperature and sea ice analysis (OSTIA) system. *Remote Sensing of Environment*, *116*, 140–158. https://doi.org/10.1016/j.rse.2010.10.017

Dussin, R., Barnier, B., Brodeau, L., & Molines, J. (2018). The making of the Drakkar forcing set DFS5 (Tech. Rep.). *Zenodo*. https://doi.org/10.5281/zenodo.1209243

Evensen, G. (2009). *Data assimilation*. Springer.

Fablet, R., Amar, M. M., Febvre, Q., Beauchamp, M., & Chapron, B. (2021). End-to-end physics-informed representation learning for satellite ocean remote sensing: Applications to satellite altimetry and sea surface currents. *ISPRS Annals of the Photogrammetry, Remote Sensing and Spatial Information Sciences*, *V-3–2021*, 295–302. https://doi.org/10.5194/isprs-annals-V-3-2021-295-2021

Fablet, R., Chapron, B., Drumetz, L., Memin, E., Pannekoucke, O., & Rousseau, F. (2021). Learning variational data assimilation models and solvers. *Journal of Advances in Modeling Earth Systems*, *13*(10), e2021MS002572. https://doi.org/10.1029/2021MS002572

Fablet, R., Febvre, Q., & Chapron, B. (2023). Multimodal 4DVarNets for the reconstruction of sea surface dynamics from SST-SSH synergies. *IEEE Transactions on Geoscience and Remote Sensing*, *61*, 1–14. https://doi.org/10.1109/TGRS.2023.3268006

Fablet, R., Verron, J., Mourre, B., Chapron, B., & Pascual, A. (2018). Improving mesoscale altimetric data from a multitracer convolutional processing of standard satellite-derived products. *IEEE Transactions on Geoscience and Remote Sensing*, *56*(5), 2518–2525. https://doi.org/10.1109/TGRS.2017.2750491

Fablet, R., Viet, P. H., & Lguensat, R. (2017). Data-driven models for the spatio-temporal interpolation of satellite-derived SST fields. *IEEE Trans. on Computational Imaging*, *3*(4), 647–657. https://doi.org/10.1109/TCI.2017.2749184

Fablet, R., & Zhu, D. (2023). 4DVarNet-UV-GF: July 23, 2023 (Vesion 0.3) [Software]. *Zenodo*. https://doi.org/10.5281/zenodo.8083903

Febvre, Q., Fablet, R., Sommer, J. L., & Ubelmann, C. (2022). Joint calibration and mapping of satellite altimetry data using trainable variational models. In *Proceedings of IEEE ICASSP* (pp. 1536–1540). (ISSN: 2379-190X). https://doi.org/10.1109/ICASSP43922.2022.9746889

Febvre, Q., Sommer, J., Ubelmann, C., & Fablet, R. (2023). Training neural mapping schemes for satellite altimetry with simulation data. *arXiv:2309.14350*. https://doi.org/10.48550/arXiv.2309.14350

Fujii, Y., Rémy, E., Zuo, H., Oke, P., Halliwell, G., Gasparin, F., et al. (2019). Observing system evaluation based on ocean data assimilation and prediction systems: On-going challenges and a future vision for designing and supporting ocean observational networks. *Frontiers in Marine Science*, *6*. https://doi.org/10.3389/fmars.2019.00417

Gaultier, L., Ubelmann, C., & Fu, L.-L. (2015). The challenge of using future SWOT data for oceanic field reconstruction. *Journal of Atmospheric and Oceanic Technology*, *33*(1), 119–126. https://doi.org/10.1175/JTECH-D-15-0160.1

George, T., Manucharyan, G., & Thompson, A. (2021). Deep learning to infer eddy heat fluxes from sea surface height patterns of mesoscale turbulence. *Nature Communications*, *12*(1), 800. https://doi.org/10.1038/s41467-020-20779-9

Guimbard, S., Reul, N., Chapron, B., Umbert, M., & Maes, C. (2017). Seasonal and interannual variability of the Eastern Tropical Pacific Fresh Pool. *Journal of Geophysical Research: Oceans*, *122*(3), 1749–1771. https://doi.org/10.1002/2016JC012130

Hospedales, T., Antoniou, A., Micaelli, P., & Storkey, A. (2020). Meta-learning in neural networks: A survey. *arXiv:2004.05439*.

Isern-Fontanet, J., Chapron, B., Lapeyre, G., & Klein, P. (2006). Potential use of microwave sea surface temperatures for the estimation of ocean currents. *Geophysical Research Letters*, *33*(L24608). https://doi.org/10.1029/2006GL027801

Isern-Fontanet, J., Shinde, M., & Andersson, C. (2014). On the transfer function between surface fields and the geostrophic stream function in the Mediterranean Sea. *Journal of Physical Oceanography*, *44*(5), 1406–1423. https://doi.org/10.1175/JPO-D-13-0186.1

Jones, M., Allen, M., Guymer, T., & Saunders, M. (1998). Correlations between altimetric sea surface height and radiometric sea surface temperature in the South Atlantic. *Journal of Geophysical Research*, *103*(C4), 8073–8087. https://doi.org/10.1029/97JC02177

Klein, P., & Hua, L. (1990). The mesoscale variability of the sea surface temperature: An analytical and numerical model. *Journal of Marine Research*, *48*(4), 729–763. https://doi.org/10.1357/002224090784988700

Lafon, N., Fablet, R., & Naveau, P. (2023). Uncertainty quantification when learning dynamical models and solvers with variational methods. *Journal of Advances in Modeling Earth Systems*, *15*(11), e2022MS003446. https://doi.org/10.1029/2022MS003446

LeCun, Y., Bengio, Y., & Hinton, G. (2015). Deep learning. *Nature*, *521*(7553), 436–444. https://doi.org/10.1038/nature14539

Le Goff, C., Fablet, R., Autret, E., Tandeo, P., & Chapron, B. (2016). Spatio-temporal decomposition of satellite-derived SST-SSH fields: Links between surface data and ocean interior dynamics in the Agulhas region. *IEEE Journal of Selected Topics in Applied Earth Observations and Remote Sensing*, *9*(11), 5106–5112. https://doi.org/10.1109/JSTARS.2016.2605040

Le Guillou, F., Metref, S., Cosme, E., Ubelmann, C., Ballarotta, M., Le Sommer, J., & Verron, J. (2020). Mapping altimetry in the forthcoming SWOT era by back-and-forth nudging a one-layer quasigeostrophic model. *Journal of Atmospheric and Oceanic Technology*, *38*(4), 697–710. https://doi.org/10.1175/jtech-d-20-0104.1

Lguensat, R., Tandeo, P., Aillot, P., & Fablet, R. (2017). The analog data assimilation. *Monthly Weather Review*, *145*(10), 4093–4107. https://doi.org/10.1175/mwr-d-16-0441.1

Madec, G., Bourdalle-Badie, R., Chanut, J., Clementi, E., Coward, A., Ethe, C., et al. (2022). NEMO ocean engine Tech. Report. *Zenodo*. https://doi.org/10.5281/zenodo.6334656

Mahadevan, A., & Tandon, A. (2006). An analysis of mechanisms for submesoscale vertical motion at ocean fronts. *Ocean Modelling*, *14*(3), 241–256. https://doi.org/10.1016/j.ocemod.2006.05.006

Manucharyan, G. E., Siegelman, L., & Klein, P. (2021). A deep learning approach to spatiotemporal sea surface height interpolation and estimation of deep currents in geostrophic ocean turbulence. *Journal of Advances in Modeling Earth Systems*, *13*(1), e2019MS001965. https://doi.org/10.1029/2019MS001965

Martinez, E., Brini, A., Gorgues, T., Drumetz, L., Roussillon, J., Tandeo, P., et al. (2020). Neural network approaches to reconstruct phytoplankton time-series in the global ocean. *Remote Sensing*, *12*(24), 4156. https://doi.org/10.3390/rs12244156

McWilliams, J., Gula, J., & Molemaker, M. (2019). The gulf stream north wall: Ageostrophic circulation and frontogenesis. *Journal of Physical Oceanography*, *49*(4), 893–916. https://doi.org/10.1175/JPO-D-18-0203.1

Moore, A., Martin, M., Akella, S., Arango, H., Balmaseda, M., Bertino, L., et al. (2019). Synthesis of ocean observations using data assimilation for operational, real-time and reanalysis systems: A more complete picture of the state of the Ocean. *Frontiers in Marine Science*, *6*. https://doi.org/10.3389/fmars.2019.00090

Nonnenmacher, M., & Greenberg, D. (2021). Deep Emulators for differentiation, forecasting, and parametrization in Earth science simulators. *Journal of Advances in Modeling Earth Systems*, *13*(7), e2021MS002554. https://doi.org/10.1029/2021MS002554

O'Carroll, A., Armstrong, E., Beggs, H., Bouali, M., Casey, K., Corlett, G. K., et al. (2019). Observational needs of sea surface temperature. *Frontiers in Marine Science*, *6*. https://doi.org/10.3389/fmars.2019.00420

Okubo, A. (1970). Horizontal dispersion of floatable particles in the vicinity of velocity singularities such as convergences. *Deep-Sea Research*, *17*(3), 445–454. https://doi.org/10.1016/0011-7471(70)90059-8

Puissant, A., El Hourany, R., Charantonis, A., Bowler, C., & Thiria, S. (2021). Inversion of phytoplankton pigment vertical profiles from satellite data using machine learning. *Remote Sensing*, *13*(8), 1445. https://doi.org/10.3390/rs13081445

Reul, N., Chapron, B., Lee, T., Donlon, C., Boutin, J., & Alory, G. (2014). Sea surface salinity structure of the meandering Gulf Stream revealed by SMOS sensor. *Geophysical Research Letters*, *41*(9), 3141–3148. https://doi.org/10.1002/2014GL059215

Rio, M.-H., Santoleri, R., Bourdalle-Badie, R., Griffa, A., Piterbarg, L., & Taburet, G. (2016). Improving the altimeter-derived surface currents using high-resolution sea surface temperature data: A feasability study based on model outputs. *Journal of Atmospheric and Oceanic Technology*, *33*(12), 2769–2784. https://doi.org/10.1175/JTECH-D-16-0017.1

Roemmich, D., Alford, M., Claustre, H., Johnson, K., King, B., Moum, J., et al. (2019). On the future of argo: A global, full-depth, multi-disciplinary array. *Frontiers in Marine Science*, *6*. https://doi.org/10.3389/fmars.2019.00439

Shorten, C., & Chin, T. (2019). A survey on image data augmentation for deep learning. *Journal of Big Data*, *6*(1), 60. https://doi.org/10.1186/s40537-019-0197-0

Storto, A., Alvera-Azcarate, A., Balmaseda, M., Barth, A., Chevallier, M., Counillon, F., et al. (2019). Ocean reanalyses: Recent advances and unsolved challenges. *Frontiers in Marine Science*, *6*. https://doi.org/10.3389/fmars.2019.00418

Storto, A., Falchetti, S., Oddo, P., Jiang, Y., & Tesei, A. (2020). Assessing the impact of different ocean analysis schemes on oceanic and underwater acoustic predictions. *Journal of Geophysical Research*, *125*(7), e2019JC015636. https://doi.org/10.1029/2019JC015636

Storto, A., Magistris, G., Falchetti, S., & Oddo, P. (2021). A neural network–based observation operator for coupled ocean–Acoustic variational data assimilation. *Monthly Weather Review*, *149*(6), 1967–1985. https://doi.org/10.1175/MWR-D-20-0320.1

Sun, L., Penny, S. G., & Harrison, M. (2022). Impacts of the Lagrangian data assimilation of surface drifters on estimating ocean circulation during the Gulf of Mexico Grand Lagrangian Deployment. *Mont. Weath. Rev.*, *150*(4), 949–965. https://doi.org/10.1175/MWR-D-21-0123.1

Taburet, G., Sanchez-Roman, A., Ballarotta, M., Pujol, M.-I., Legeais, F., Fournier, F., et al. (2019). DUACS DT2018: 25 years of reprocessed sea level altimetry products. *Ocean Science*, *18*(5), 1207–1224. https://doi.org/10.5194/os-15-1207-2019

Tandeo, P., Chapron, B., Ba, S., Autret, E., & Fablet, R. (2013). Segmentation of mesoscale ocean surface dynamics using satellite SST and SSH observations. *IEEE Transactions on Geoscience and Remote Sensing*, *52*(7), 4227–4235. https://doi.org/10.1109/TGRS.2013.2280494

Tilstone, G., Pardo, S., Dall'Olmo, G., Brewin, R., Nencioli, F., Dessailly, D., et al. (2021). Performance of ocean colour chlorophyll a algorithms for Sentinel-3 OLCI, MODIS-Aqua and Suomi-VIIRS in open-ocean waters of the Atlantic. *Remote Sensing of Environment*, *260*, 112444. https://doi.org/10.1016/j.rse.2021.112444

Turiel, A., Sole, J., Nieves, V., Ballabrera-Poy, J., & Garcia-Ladona, E. (2008). Tracking oceanic currents by singularity analysis of Microwave Sea Surface Temperature images. *Remote Sensing of Environment*, *112*(5), 2246–2260. https://doi.org/10.1016/j.rse.2007.10.007

Ubelmann, C., Klein, P., & Fu, L.-L. (2014). Dynamic interpolation of sea surface height and potential applications for future high-resolution altimetry mapping. *Journal of Atmospheric and Oceanic Technology*, *32*(1), 177–184. https://doi.org/10.1175/JTECH-D-14-00152.1

Uchida, T., Le Sommer, J., Stern, C., Abernathey, R. P., Holdgraf, C., Albert, A., et al. (2022). Cloud-based framework for inter-comparing submesoscale-permitting realistic ocean models. *Geoscientific Model Development*, *15*(14), 5829–5856. https://doi.org/10.5194/gmd-15-5829-2022

Vient, J., Jourdin, F., Fablet, R., Mengual, B., Lafosse, L., & Delacourt, C. (2021). Data-driven interpolation of sea surface suspended concentrations derived from ocean colour remote sensing data. *Remote Sensing*, *13*(17), 3537. https://doi.org/10.3390/rs13173537

Villas Boas, A., Ardhuin, F., Ayet, A., Bourassa, M., Brandt, P., Chapron, B., et al. (2019). Integrated observations of global surface winds, currents, and waves: Requirements and challenges for the Next decade. *Frontiers in Marine Science*, *6*. https://doi.org/10.3389/fmars.2019.00425

Wang, H., Grisouard, N., Salehipour, H., Nuz, A., Poon, M., & Ponte, A. (2022). A deep learning approach to extract internal tides Scattered by geostrophic turbulence. *Geophysical Research Letters*, *49*(11), e2022GL099400. https://doi.org/10.1029/2022GL099400

Weiss, J. (1991). The dynamics of enstrophy transfer in two-dimensional hydrodynamics. *Physica D: Nonlinear Phenomena*, *48*(2), 273–294. https://doi.org/10.1016/0167-2789(91)90088-q

Xu, Y., & Fu, L.-L. (2012). The effects of altimeter Instrument noise on the estimation of the wavenumber Spectrum of sea surface height. *Journal of Physical Oceanography*, *42*(12), 2229–2233. https://doi.org/10.1175/JPO-D-12-0106.1

Yurovskaya, M., Kudryavtsev, V., Chapron, B., & Collard, F. (2019). Ocean surface current retrieval from space: The Sentinel-2 multispectral capabilities. *Remote Sensing of Environment*, *234*, 111468. https://doi.org/10.1016/j.rse.2019.111468

Zhu, D., & Fablet, R. (2023). 2023-OSSE-SSC-NATL60-GF: June 27, 2023 [Dataset and Benchmark]. *Zenodo*. https://doi.org/10.5281/zenodo.8076318